



Characteristics of a fracture network surrounding a hydrothermally altered shear zone from geophysical borehole logs

Eva Caspari^{1,2}, Andrew Greenwood^{1,2}, Ludovic Baron¹, Daniel Egli³, Enea Toschini¹, Kaiyan Hu^{1,4}, and Klaus Holliger^{1,5}

¹Institute of Earth Sciences, University of Lausanne, Lausanne Switzerland

²Chair of Applied Geophysics, Montanuniversitaet Leoben, Austria

³Institute of Geological Sciences, University of Bern, Bern, Switzerland

⁴Department of Geophysics, Peking University, Beijing, China

⁵School of Earth Sciences, Zhejiang University, Hangzhou, China

Correspondence: Eva Caspari (Eva.Caspari@unil.ch, eva.caspari@unileoben.ac.at)

Abstract. Hydrothermally active and altered fault/shear zones in crystalline rocks are of practical importance because of their potential similarities with petrothermal reservoirs and exploitable natural hydrothermal systems. The petrophysical and hydraulic characterization of such structures is therefore of significant interest. Here, we report the results of corresponding investigations on a prominent shear zone of this type located in the crystalline Aar massif of the central Swiss Alps. A shallow borehole was drilled, which acutely intersects the core of the shear zone and is entirely situated in its surrounding damage zone. The focus of this study is a detailed characterization of this damage zone based on geophysical borehole measurements. For this purpose, a comprehensive suite of borehole logs, comprising passive and active nuclear, full-waveform sonic, resistivity, self-potential, optical televiewer, and borehole radar data, was collected. The migrated images of the borehole radar reflection data together with the optical televiewer data reveal a complicated network of intersecting fractures in the damage zone. Consequently, the associated petrophysical properties, notably the sonic velocities and porosities, are distinctly different from intact granitic formations. Cluster analyses of the borehole logs in combination with the structural interpretations of the optical televiewer data illustrate that the variations in the petrophysical properties are predominantly governed by the intense brittle deformation. The imaged fracture network and the high-porosity zones associated with brittle deformation represent the main flow pathways. This interpretation is consistent with the available geophysical measurements as well as the analyses of the retrieved core material. Furthermore, the interpretation of the self-potential and fluid resistivity log data suggests a compartmentalized hydraulic behavior, as evidenced by inflows of water into the borehole from different sources, which is likely to be governed by the steeply dipping structures.

1 Introduction

As opposed to their sedimentary counterparts, crystalline rocks tend to be characterized by very small matrix porosities and hence fluid pathways are mostly associated with brittle deformation structures at scales ranging from micrometers to kilometers, such as fractures and fault/shear zones as well as their associated damage zones (e.g., Brace, 1980; Barton et al., 1995; Evans et al.,



1997; Caine et al., 1996; Faulkner and Armitage, 2013) . These structures do not only dominate the hydraulic behavior, but also act as zones of weakness and thus substantially affect the mechanical behavior of the rock mass. For many applications, a thorough understanding of the mechanical and hydraulic characteristics of the examined rock volume is critical. For example, in tunneling operations and nuclear waste storage repositories, fractures provide undesired zones of weakness and hydraulic conductivity, while the same characteristics represent desirable features for the exploration and creation of enhanced geothermal systems (e.g., Evans et al., 2005; Loew et al., 2010; Stephens et al., 2015; Regenauer-Lieb et al., 2015). The overarching importance of fractures and fracture networks inspired a wealth of research on their geometrical, hydraulic, and mechanical properties (e.g., Barton et al., 1995; Nelson, 2001; Berkowitz, 2002; Valley, 2007; Liu and Martinez, 2014). Although it has been shown that geophysical borehole logs can provide petrophysical properties of individual fractures and fractures networks (e.g., Prioul and Jocker, 2009; Hobday and Worthington, 2012; Barbosa et al., 2019), so far only a few studies systematically analyze fracture systems in crystalline rocks based on geophysical borehole logs (e.g., Paillet, 1994; Townend et al., 2013).

The structure of interest in this study is the Grimsel Breccia Fault (GBF), a major WSW-ENE striking sub-vertical brittlely overprinted shear zone in the Southwestern Aar Granite of the central Swiss Alps, which exhibits evidence of both fossil and active hydrothermal activity (Hofmann et al., 2004; Belgrano et al., 2016). To this end, a shallow borehole has been drilled into the GBF, which acutely intersects the main brecciated fault core and is entirely situated in its surrounding damage zone. A comprehensive suite of geophysical borehole logs, comprising passive and active nuclear, full-waveform sonic (FWS), resistivity, self-potential (SP), and borehole radar (BHR) measurements, were collected in 2015, 2016 and 2017. In a previous study (Greenwood et al., 2019), hydrophone vertical seismic profiling (VSP) data in combination with some of the borehole log data were used to image and characterize the main fault core of the GBF. The resulting seismic image allowed to delineate the targeted zone and numerous tube waves in the hydrophone VSP data could be linked to hydraulically open fractures in the damage zone around the fault core. A quantitative analysis of the amplitudes of the hydrophone VSP data in terms of hydraulic conductivity was, however, not possible due to the abundance of tube wave events and the resulting interference of the various parts of the recorded seismic wavefield. Egli et al. (2018) performed a structural characterization of the GBF system and its evolution with a specific focus on porosity, permeability, fracture distribution, and fluid flow reconstruction based on the combined analysis of drill cores, optical televiewer (OTV) data, and geological mapping. Building on the results of these previous works, the focus of this study is a detailed characterization of the fracture network in the damage zone of the main fault core from geophysical borehole log data with a particular focus on the network's geometrical and petrophysical properties as well as the links of the latter to brittle deformation.

In contrast to the classically utilized OTV data and core samples, which identify the location, orientation, and dip of fractures along the borehole (e.g., Genter et al., 1997; Valley, 2007), geophysical borehole logs sample a more representative volume of the fractured rock mass away from the immediate vicinity of the borehole and, as such, are essential in intervals of core loss (e.g., Ellis and Singer, 2007). However, a drawback of the larger sampling volume is that individual fractures and other smaller-scale structures tend to be difficult to discriminate and detect. Moreover, geophysical borehole log measurements



tend to be sensitive to a combination of petrophysical properties, thus rendering quantitative estimations from single log-type measurements difficult and ambiguous. Correspondingly, an integrated workflow utilizing a variety of geophysical borehole log measurements is necessary to mitigate these ambiguities. Such an integrated analysis, in combination with evidence from OTV and core data, is used in this study to constrain geometrical and petrophysical properties of the GBF damage zone. BHR reflection data are employed to image the damage zone and to infer the geometrical characteristics of its fracture network. To analyze the distribution of petrophysical properties in the damage zone and their link to brittle deformation, a cluster analysis is performed for a selection of geophysical borehole logs. Finally, to shed light on the hydraulic characteristics of the GBF, we examine SP and fluid resistivity log data. To test and verify our findings, we assess their compatibility with the detailed structural characterization of Egli et al. (2018) and the results of previous studies by Belgrano et al. (2016) and Cheng and Renner (2017) on the hydraulic nature of the GBF. The paper starts with a brief description of the geological setting, the challenges associated with the acquisition of the geophysical borehole logs in the intensely fractured crystalline environment, and their resulting impact on the quality and reliability of the data.

2 Geological setting and borehole conditions

The GBF is a major WSW-ENE striking sub-vertical shear zone in the Southwestern Aar Granite, which has been exhumed from 3 - 4 km depth and brittlely overprinted. The GBF exhibits both fossil and current hydrothermal activity (Hofmann et al., 2004; Belgrano et al., 2016), the latter being evidenced by warm springs in the village of Gletsch (~18°C) and in the Transitzgas AG tunnel ~200 m (up to 28°C) below the Grimsel Pass (Hofmann et al., 2004; Sonney and Vuataz, 2008), which is the site for this study (Fig. 1). The hydrothermal water in the tunnel consists to approximately equal parts of recent meteoric components and older geothermal components, which reached circulation depths of several kilometers and maximum temperatures of 110-120°C (Waber et al., 2017).

The location of the GDP1 borehole and a schematic cross-section are shown in Fig. 1, which also illustrates the extreme topographic relief of the area. The borehole is orientated approximately SSE, orthogonal to geological strike, with a vertical deviation of 24°, and acutely intersects the GBF main breccia core between 82 and 86 m borehole depth. The GDP1 borehole was diamond-drilled with a so-called HQ bit (96 mm outer diameter, 76 mm inner diameter) to a length of 125.3 m. During the drilling operations, fluid circulation was lost at 76 m borehole depth and, hence, the borehole was cemented and re-drilled between 71 and 76 m depth. Due to the intense fracturing, breakouts are encountered along the entire length of the borehole and inherently affect the quality of the logging data.

A list of all geophysical borehole datasets collected along the GDP1 borehole during 2015, 2016, and 2017 is shown in Table 1 together with the respective condition of the borehole at the time of their acquisition. Throughout this paper, all data are referred to and displayed with regard to measured depth along the borehole track. The most complete dataset was collected in 2015 directly after drilling under open borehole conditions. It comprises OTV, borehole caliper, passive and active nuclear,

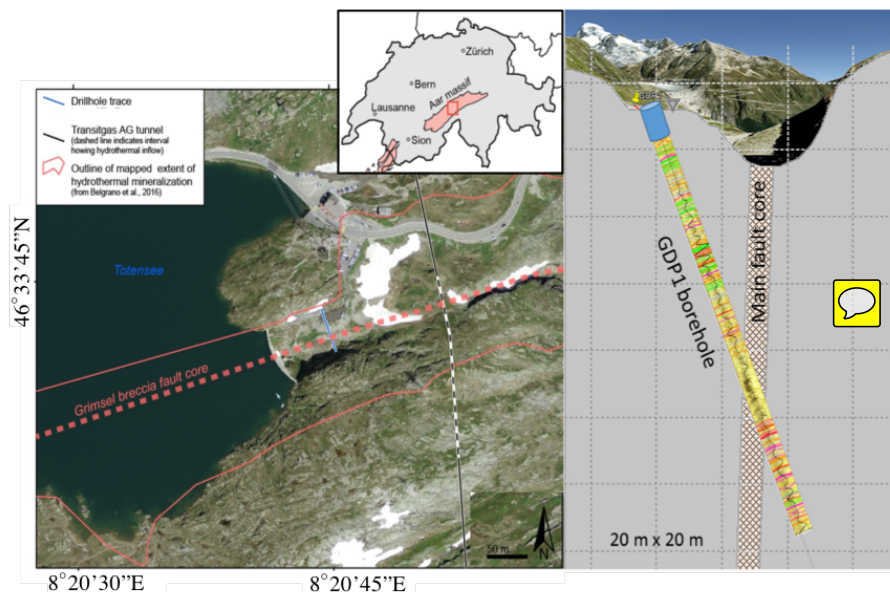


Figure 1. a) Aerial image (Source: Federal Office of Topography www.swisstopo.ch) of the Grimsel Pass showing the trace of the GDP1 borehole, the extent of mineralized outcrops associated with the GBF (Belgrano et al., 2016), and the location of the Transitgas AG tunnel with the interval of active hydrothermal inflow marked by the white stippled line (modified from Egli et al. (2018)). b) Schematic cross-section through the plane of the borehole intersecting GBF showing the extreme topographic relief in conjunction with the location and orientation of the borehole (modified from Greenwood et al. (2019)).

90 electrical resistivity, SP, temperature, and multiple centre frequency FWS logs as well as constant offset BHR, ambient flowmeter, and periodic pumping test measurements.

After completion of the drilling operations, water from the adjacent lake was pumped into the borehole to flush out the polymer-based drilling mud and to enable OTV measurements. Although, the water in the borehole cleared up, remnants of the drilling fluid within the adjacent formation were likely to be present throughout the 2015 logging campaign. As a consequence, the SP data acquired in 2015 differ significantly from those measured in 2016 and 2017 since the polymer-based drilling mud changed the viscosity and the chemical composition of the pore fluid in the rock volume with regard to its ambient state. In addition to this, the 2015 SP data were also affected by changes in the flow regime in and around the borehole induced by the pumping of lake water. In the following, we therefore only consider the SP data acquired in 2016 and 2017. The addition of the lake water and the remnant presence of drilling mud also affected the 2015 electrical resistivity measurements. These were therefore repeated in 2016 and 2017 through the slotted PVC casing, which was installed to prevent borehole collapse. To analyze the effects of this casing as well as for data calibration purposes, a small section at the bottom of the borehole was re-measured under open borehole conditions in 2017. Details with regard to the data corrections applied to remove the casing

100



Table 1. List of borehole measurements performed in 2015, 2016, and 2017

Borehole tools	2015 (open)	2016 (cased: slotted PVC)	2017 (cased: slotted PVC)	2017 (open 108-121 m)
Polyprobe (2PEA/2PGA- 1000 F)	Water Table: 8 m	Water Table: 31m	Water Table: 33 m	
Natural Gamma (NG)	x	x	x	x
Resistivity (N08, N16, N32, N64)	x Polymer drilling mud and pumping of lake water	x Casing corrected	x Casing corrected N32, N64: noisy	x
Single-point resistance (SPR)	x Disturbed borehole cond.	x Noisy	x Noisy	x
Self-potential (SP)	x Disturbed borehole cond.	x Casing corrected	x Casing corrected	x
Temperature	x Disturbed borehole cond.	x	x	x
Fluid properties (STS data logger DLN 70)				
Temperature		x Undisturbed		
Fluid resistivity		x Undisturbed		
EM Flowmeter (9722 Century)	x			
Periodic pumping test*	x			
Full-waveform sonic (FWS) (Mount Sopris, 2SAA-1000)	Water Table: 33 m			
Continuous 25 kHz	x High gain, 2 receivers	x High gain, 3 receivers		
Continuous 2, 5, 10 kHz	x Low gain, 2 receivers			
Static multi frequency	x Selected positions	x Selected positions	x Selected positions	
Borehole georadar (BHR) (MALÅ 100 MHz Slimhole antenna)	x center-to-center antenna separation of 2.72 m	x center-to-center antenna separation of 2.72 m		
Nuclear				
Gamma-Gamma (Mount Sopris KLP - 2780)	x			
Neutron-Neutron (Mount Sopris LLP-2676)	x			
Caliper (Mount Sopris 2SNA-1000)	x			
Optical televiewer (ALT, OBI-40)	x Multiple runs			

*Cheng and Renner (2017)

effects are given in Appendix B and Toschini (2018).



BHR measurements were repeated in 2016, as no zero-time correction was available for the data collected in 2015. However, the 2015 data were acquired with a smaller spatial sampling interval and thus produce more coherent signals. For this reason, we utilize the 2016 data for calibration of the 2015 dataset, which we then consider for the remainder of the paper. Corresponding details are given in Appendix A . Additionally, more detailed temperature and fluid resistivity measurements were
110 conducted in 2016. High-frequency (25 kHz nominal center frequency), high-gain three-receiver FWS data were acquired in
2016 for more reliable and robust compressional (P) and shear (S) wave velocity estimations by semblance analysis (Hornby,
1989). In the intensely fractured zones, especially around the main fault core, the first arrivals are, however, still very weak thus
making reliable velocity estimations very difficult due to the inherent uncertainty and local variability of the picks. Therefore,
the P- wave velocity estimates are smoothed and the S-wave velocity is entirely discarded in this zone. Everywhere else, the P-
115 and S-wave estimates are reasonably robust.

Overall, the logging data are affected by strong borehole breakouts, which complicates their quantitative analysis. The
breakouts are primarily due to the intensely fractured nature of the rock volume rather than being purely drilling-induced
damage. Most of the breakouts can indeed be associated with distinct fractures or cataclastic features along the borehole track
120 and thus present structural and petrophysical indicators in their own right. Geochemically the rock mass of the damage zone
surrounding the GBF core is relatively homogeneous consisting of metagranite. The main heterogeneities are variations in
fabric, ranging from granitic through gneissic all the way to mylonitic as well as fractured and cataclastic zones, which are due
to different degrees of ductile and/or brittle deformation (Egli et al., 2018). In the following, we seek to link these geological
features inferred from the OTV and core data to the responses of the geophysical borehole logs. In a first step, we utilize
125 the BHR data to image the fracture network situated in the damage zone. Then, the response of selected borehole log data is
compared to different degrees of deformation encountered.

3 Borehole radar reflection data: Imaging of the fracture network

In contrast to most other geophysical borehole logging techniques, which have a relatively limited range of investigation, the
BHR reflection method allows to image individual fractures, clusters of fractures, and clataclastic zones outside of the immedi-
130 ate vicinity of the borehole (e.g., Olsson et al., 1992; Dorn et al., 2012). As such, these data are much less affected by borehole
breakouts than most other logging data. In the considered setting, the reflection coefficient is governed by the pronounced
contrast of the dielectric permittivity between the host rock and the fluid-filled fractures, while the bulk conductivity of the
rock volume determines the attenuation of the BHR signals. This, in turn, makes resistive crystalline environments ideal sites
for BHR measurements in general and for imaging fractures in particular. In the following, we first describe the processing of
135 the BHR data and then proceed to analyze the migrated images.



3.1 Data processing

Steeply dipping reflections are already visible in the raw data (Fig. 2a). To extract these reflections, the direct wave is removed via an alpha-trimmed 2D spatial filter after applying a static correction to flatten out the first arrivals. Subsequently, this static correction is reversed to place the reflections back into their original position (Fig. 2b). Since, the dataset was acquired with
140 omni-directional antennae, we can only determine the relative dip of the reflectors with respect to the borehole trajectory. It is not possible to constrain the azimuthal orientation of the reflectors. However, the OTV data indicate that the azimuths of most brittle and ductile structural features are constrained to one quadrant (Fig. 2c). Hence, it is justified to treat the reflections as up- and down-going wavefields originating at the same reflectors. Correspondingly, these up- and down-going wavefields are separated by f-k quadrant filters, then migrated using pre-stack Kirchhoff time-migration and converted to distance using a
145 constant average velocity. Since the prevailing geological structure is near-vertical, the velocity is varying laterally, which was at least partially accounted for in the pre-stack time-migration process by a laterally varying velocity model derived from the first arrivals. Pertinent details of the processing and imaging flow applied to the BHR reflection data are given in Table 2

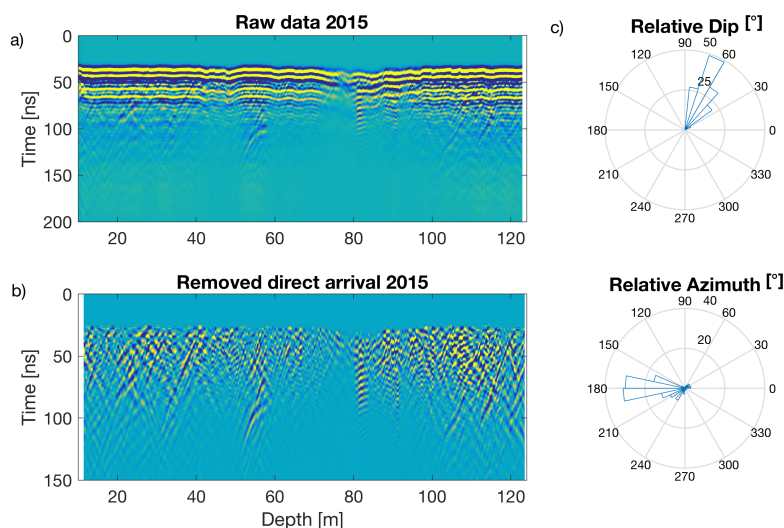


Figure 2. a) Raw BHR reflection data and b) after removal of the direct wave and reversed static corrections. c) Relative dips and azimuths of fractures identified in the OTV data.

3.2 Estimation of fracture dip

150 Figure 3a shows the final migrated and distance-converted BHR reflection image, which consists of the up- and down-going wavefields, plotted in positive distance orthogonally from the borehole trajectory. We observe an abundance of reflections, most of which intercept the borehole wall. It is straightforward to calculate the relative dip of these events. In zones of low



Table 2. Processing and imaging of BHR reflection data

Processing	
Removal of direct wave:	Static correction, 2D alpha-trimmed filter, reverse static correction, Geometrical spreading correction
Separation of up- and down-going wavefields:	f - k quadrant filter
Noise removal:	Small window 2D median temporal and spatial filter Low-pass filter
Imaging	
	2D pre-stack Kirchhoff time-migration with laterally varying velocity model
	Amplitude balancing
	Time-to-distance conversion (constant velocity)

attenuation, which correspond to large first-cycle amplitudes of the direct wave in Fig. 3b, some of these events can be traced to distances of up to 10 m from the borehole. These zones are representative of more intact rock. Conversely, high signal
155 attenuation, characterized by low first-cycle amplitudes in Fig. 3c, occurs in zones of intense brittle deformation, such as, for example, in the fault core and its vicinity.

From the image shown in Fig. 3a, we manually pick the dips of the brightest reflections as well as some of the weaker cross-cutting events to capture the variety of dips encountered. A representative selection of the picked events is superimposed
160 on the image as straight red lines and their locations with regard to the borehole track and their dips are illustrated in Fig. 3b by red dots encircled in blue. All picked events are plotted in Fig. 3b, and their values are compared to the fracture dips inferred from the OTV data, which are shown as turquoise dots whose diameter is indicative of the fracture aperture (Egli et al., 2018). Following Egli et al. (2018), fractures with very large apertures are classified as cataclastic zones. Overall, the range of dip
165 angles picked from the imaged BHR reflection data is consistent with those inferred from the OTV data, although it is difficult to match individual reflection events with specific fractures in the OTV images. The reason for this is twofold: (1) Both datasets contain the signatures of an abundance of fractures, which, in turn, necessitates an inherently subjective selection, and (2) the depth locations and dips assigned to BHR reflectors might differ slightly with regard to those of the OTV data.

Nevertheless, the comparison of the two datasets confirms that in such an environment fluid-filled fractures and cataclastic
170 zones are the most likely cause of BHR reflections. The BHR reflection image allows to trace the associated brittle deformation structures several meters from the borehole into the adjacent formation. The BHR reflection image and the OTV data provide clear and consistent evidence for a dense and complex network of fluid-filled intersecting fractures and cataclastic zones above and below the main fault core. Such a network of fractures provides effective fluid pathways through the otherwise tight granitic host rock (e.g., Berkowitz, 2002).

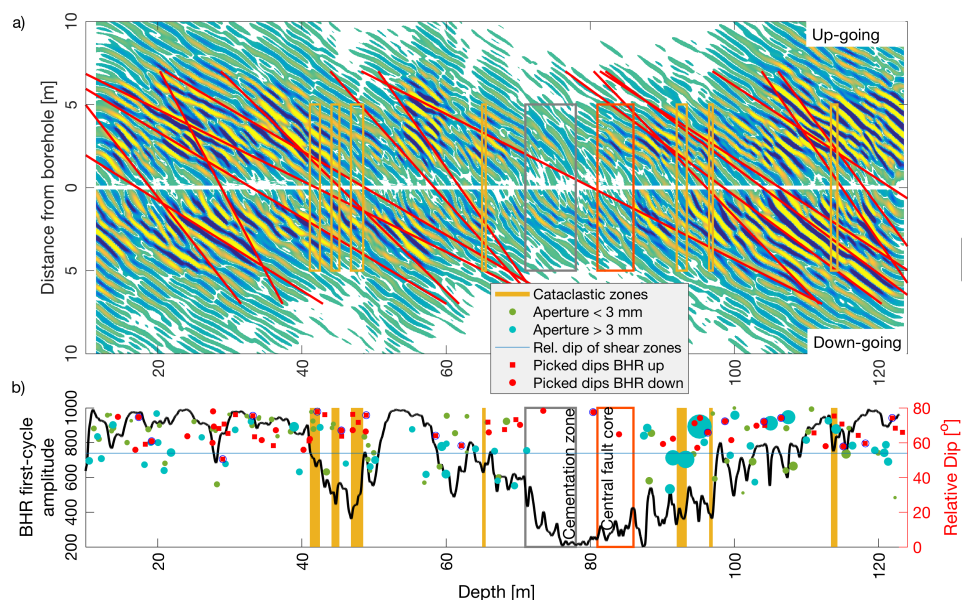


Figure 3. a) Migrated BHR image consisting of the up- and down going reflection data plotted in positive distance from the borehole trajectory. Red lines denote selected reflection events used for estimating the dips and locations of the associated fractures. b) Maximum first-cycle amplitude of BHR first arrivals (black line), relative dip of fractures from OTV data (turquoise dots) and relative dips picked from the depth-converted BHR reflection image (red dots). For the OTV data, the size of the dots is a relative measure of fracture aperture. The dips of events denoted by red lines in a) are identified by red dots encircled in blue.

175 4 Characteristics of the damage zone from geophysical logs

4.1 Full-waveform sonic data: Identification of brittle deformation zones

As illustrated by Fig. 3b, the first-cycle amplitude of the BHR first arrivals is a good proxy for the degree of brittle deformation. Similarly, FWS data are expected to be sensitive to brittle deformation as the associated wave propagation is governed by the underlying elastic and hydraulic properties of the medium. Here, we utilize the 2 kHz low-gain FWS data, which is mainly
180 sensitive to low-frequency Stoneley waves. This wave type is an interface wave traveling along the borehole wall. Its velocity depends predominately on the shear modulus of the formation and bulk modulus of the fluid. Its amplitude decreases across
compliant and hydraulically transmissive features, such as fractures and cataclastic zones, due to transmission losses, reflections, and pressure diffusion processes (e.g., Paillet, 1994). Following Paillet (1983), the local Stoneley wave energy deficit can
185 be used as an indicator for the hydraulic transmissivity of a system. For the considered data, a quantitative analysis is, however, not possible, since the data quality due to the roughness of the borehole wall caused by breakouts as well as the recording time are not sufficient and the data recorded at receiver 1 is clipped even for the lowest possible gain of the tool. Nevertheless, we can still estimate the local energy deficit of the recorded waveforms, which are dominated by Stoneley waves, and use this measure



190 as a qualitative proxy. To account for borehole breakouts, we compare the FWS data with the caliper and the Neutron-Neutron log data. While the Neutron-Neutron log is also affected by the borehole breakouts, it is primarily sensitive to the water content and thus to the porosity, which in the considered environment is dominated by fracture porosity (Egli et al., 2018).

195 In Fig. 4, we compare the aforementioned log data to the OTV-based brittle deformation data of Egli et al. (2018). Fig. 4a shows the low-gain FWS log data recorded at receiver 2 for a nominal center frequency of 2 kHz and Fig. 4b the corresponding power spectrum. The former is overlain by the caliper log and the latter by the Neutron-Neutron log. The color scale in Fig. 4a is chosen such that the primarily visible signal is the Stoneley wave. The first arrival P- and S-waves are much lower in amplitude. The local energy deficit is shown in Fig. 4c for two frequency bands and overlain with the OTV-based brittle deformation data of Egli et al. (2018). Fig. 4c also depicts the BHR first-cycle amplitude. From the FWS data, we can clearly distinguish 5 characteristic zones denoted as A through E, which also find their expressions in the first-cycle BHR amplitudes. In the following, we compare these zones to the brittle deformation data of Egli et al. (2018).

200

- Zone A consists of three cataclastic zones. The OTV image and the core material of such a cataclastic zone are shown in Fig. 4d on the left-hand side. These cataclastic zones are characterized by time-delayed, low-amplitude Stoneley waves with an energy reduction of 15% as well as low BHR amplitudes. Moreover, they find their expression as prominent anomalies in the caliper and Neutron-Neutron logs. As such, zone A is likely to represent a hydraulically transmissive interval of low shear strength and high porosity.
- Compared to zone A, zone B is characterized by a smaller energy deficit and an overriding high-frequency wave corresponding to the pseudo-Rayleigh wave, which only exists in fast formations and thus suggests a zone of higher shear strength and less brittle deformation. The latter is consistent with the high BHR amplitudes.
- Conversely, the FWS signal in zone C is dominated by low frequencies in the power spectrum with a decrease of high frequencies towards zone D and the vanishing of the pseudo-Rayleigh wave, which is indicative of a decrease in shear strength. The BHR amplitudes decrease towards zone D as well, in which the borehole collapsed and had to be cemented and redrilled. The core material in zone C, is partly non-cohesive due to intense brittle deformation, which explains the observed characteristics of the BHR amplitude and FWS data. Local vanishing of the FWS amplitudes in conjunction with anomalies in the caliper and Neutron-Neutron logs are due to individual large-aperture fractures.
- Zone D comprises the wider zone of the main fault core where most of the FWS signal is lost. One reason are the large borehole breakouts and the associated rugosity of the borehole wall, which prevents the propagation of Stoneley waves. In the upper part of this zone, a weak signal is recorded between 82 – 86 m borehole depth with a shift towards higher frequencies. This section corresponds to the GBF core consisting of fault gouge (Egli et al., 2018).

215

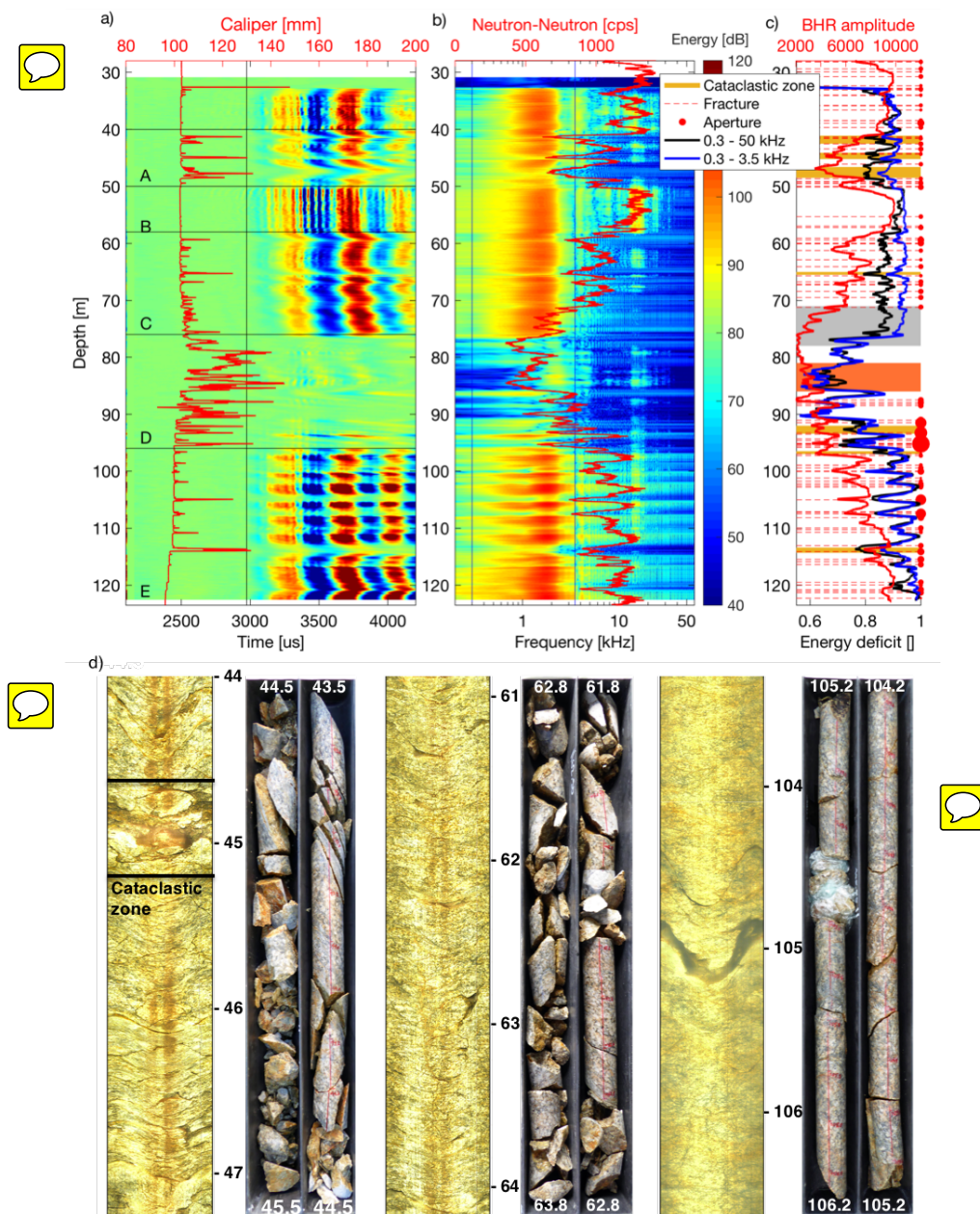


Figure 4. a) Low-gain FWS data acquired with a nominal central frequency of 2 kHz overlain by the caliper log; b) corresponding power spectrum overlain by the Neutron-Neutron log; c) relative energy deficit for two different frequency bands, one capturing the Stoneley wave and the other the complete spectrum, in conjunction with the first-cycle amplitude of the BHR direct wave and the brittle deformation data from the OTV; d) examples of brittle deformation based on a comparison of OTV data and corresponding drill core sequences.



– Finally, zone E is characterized by an alternating sequence of regions with pronounced low and high energy deficits, which is indicative of an overall rather compact rock volume with prominent isolated fractures. This interpretation is consistent with a correspondingly alternating sequence in the BHR amplitudes.

4.2 Cluster analysis

To refine the zonation identified in Fig. 4 and infer the associated petrophysical properties, we consider a pertinent selection of the logging data acquired in 2015 under open-hole conditions and in 2016 through a screened PVC casing. These are shown in Fig. 5 and include from left to right the caliper and natural gamma log, the sonic P- and S-wave velocities, the Gamma-Gamma and Neutron-Neutron logs, the BHR direct-wave velocity and amplitude, and electrical resistivity measurements. All logs are superimposed onto the brittle deformation data mapped from the OTV. The larger-scale trends of most of the logs are consistent with the previously inferred zonation A through E, which is depicted on the left-hand side of Fig. 5. The GBF fault core, which is located between 82 and 86 m borehole depth, is marked by borehole enlargements and clearly defined across the entire suite of logs. Most of the remaining anomalies observed in the borehole log data correlate with caliper enlargements, which, in turn, are associated with breakouts and can be linked to zones of the brittle deformation identified in the OTV data. In the following, we analyze the relationship between the various borehole logs and address the question whether their response can be linked to the degree of brittle deformation. To this end, we perform a cluster analysis on a selection of the log data.

In a first step, we perform a correlation analysis of the log data shown in Fig. 5. Before doing so, the datasets are normalized to account for the different unit scales. We obtain an overall good correlation between the BHR velocity and amplitude, the Neutron–Neutron, the P-wave velocity, and the normal resistivity logs. In the following, these datasets will be subjected to a cluster analysis. Although the S-wave velocity log shows a good correlation with other log data in the more intact parts of the borehole, it is not considered due to its unreliability around the main fault core. The Gamma-Gamma log is strongly affected by large borehole breakouts and shows otherwise little variation. The poor correlation of the natural gamma log with the other datasets is probably due to the fact that, in the crystalline environment, it is primarily sensitive to mineralogical alterations, which, compared to the brittle deformation structures, have a secondary effect on the other borehole logs. The BHR velocities and amplitudes are primarily sensitive to the fluid-filled porosity, and the bulk electrical conductivity, respectively, the Neutron-Neutron log to the total amount of hydrogen present in the formation, the P-wave velocity log to the mechanical properties, and the normal resistivity to the bulk resistivity.

The upper triangular region in Fig. 6 shows crossplots of the selected log data, which confirm the overall good correlation. The somewhat spurious nature of these crossplots is due to the fact that the various geophysical logs average the petrophysical properties over significantly differing support volumes. This is problematic when dealing with small-scale high-contrast features, such as fractures, embedded in an otherwise relatively homogeneous matrix. An effective way to display such datasets are histograms, as shown in the triangular region below the diagonal in Fig. 6, which clearly illustrate the overall strong correlation trends between the various datasets. The largest spread of values is observed for crossplots either containing the P-wave

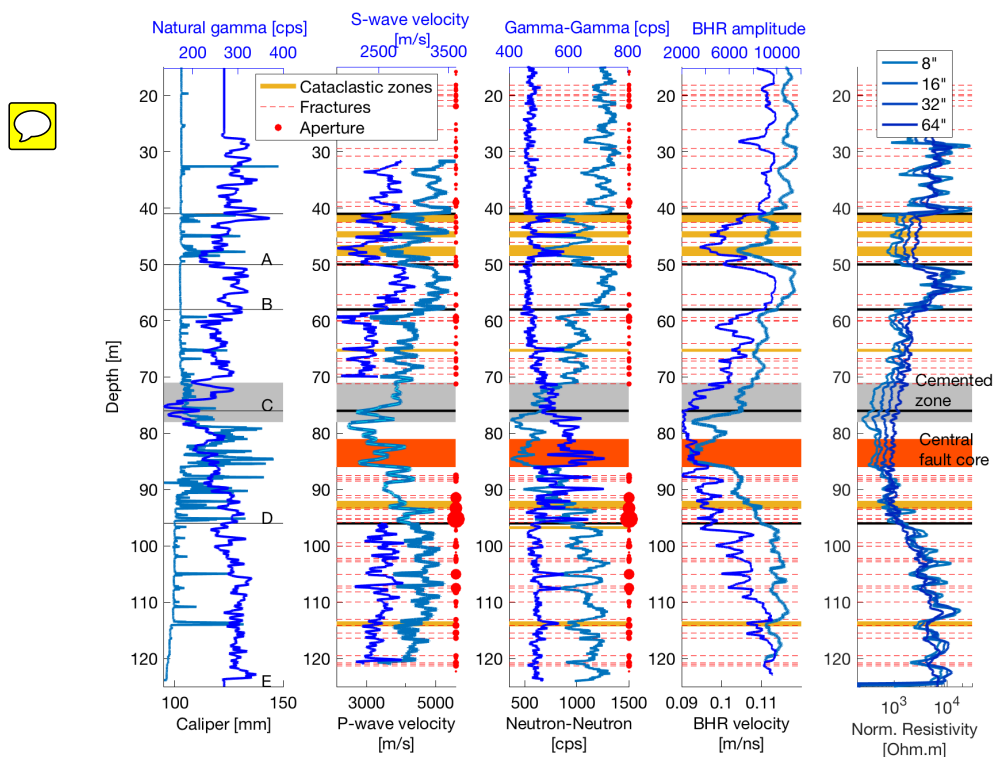


Figure 5. Representative selection of borehole log data comprising from left to right caliper, natural gamma, sonic velocity, Neutron-Neutron and Gamma-Gamma, BHR direct-wave velocity and amplitude as well as normal resistivity logs. The brittle deformation features interpreted from the OTV data (Egli et al., 2018) are superimposed on the log data. The sizes of the circles are indicative of the relative fracture apertures. Zones A through E refer to zonation shown in Fig. 4.

velocities or the BHR amplitudes, whereas the other properties show generally well-defined correlation trends.

To analyze these trends in more detail, we perform a cluster analysis using the k-means algorithm of the Matlab Statistics
 255 Toolbox with a squared Euclidian distance criterion (Arthur and Vassilvitskii, 2007). The analysis is performed on the normal-
 ized data in two subsequent steps. First, we test for the optimal number of clusters to group the data into. To do this, we use the
 so-called silhouette and gap criteria (Tibshirani et al., 2001), which both suggest an optimum of four clusters. Then, we apply
 the k-means algorithm to group the data into four clusters. The median, the 25th percentile and the outliers of each cluster and
 each petrophysical property are shown in the form of boxplots along the diagonal of Fig. 6. Across all petrophysical properties,
 260 the identified clusters show a good separation with regard to each other.

Figure 7 shows the borehole log data used for the above cluster analysis color-coded according to the four cluster groups
 identified in Fig. 6 and overlain by OTV-based brittle deformation data. Also shown is the sequence of clusters along the bore-

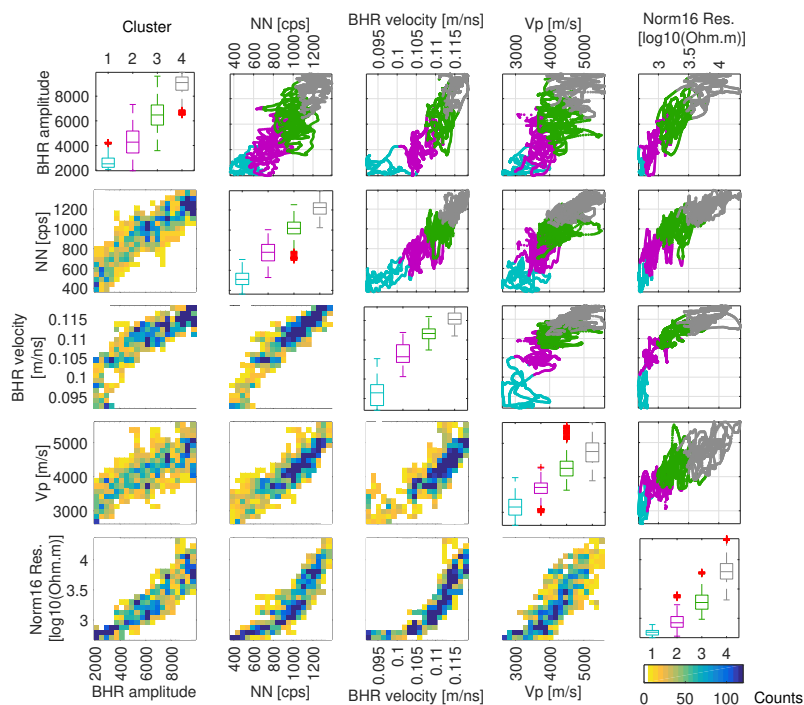


Figure 6. Lower triangle with regard to diagonal: histogram crossplots of selected borehole logs (BHR amplitude, Neutron-Neutron (NN), BHR velocity, P-wave velocity (Vp) and Normal resistivity 16'' (Norm16Res)). Upper triangle with regard to diagonal: color-coded crossplots of groups identified based on cluster analysis. The diagonal shows the corresponding cluster boxplots for each property.

hole track together with the fracture density inferred from OTV data as well as the caliper log. Comparing these various datasets
 265 allows to characterize the clusters as follows: 1) GBF fault core, 2) zones of high fracture density or cataclastic deformation, 3)
 zones of moderate fracture density or large-aperture fractures, and 4) zones of low fracture density. There is a mismatch at the
 bottom of the borehole between the cluster-based interpretation of the borehole log data and fracture density estimated from
 the OTV data. The reason is that partially and fully closed fractures are accounted for in the OTV-based fracture density, while
 the logs are largely insensitive to these types of fractures. This problem only manifests itself at the bottom of the borehole,
 270 since the occurrence of closed fractures compared to open fractures is larger in this region than elsewhere along the borehole.
 An essential result of the cluster analysis is that the signatures of the selected borehole logs as well as their interrelations are
 predominantly governed by brittle deformation in general and that the individual clusters seem to be clearly linked to the degree
 of deformation in particular. In this context, it is interesting to note that the sequence of clusters along the borehole displayed
 on the right-hand side of Fig. 7 is fully consistent the more generic zonation A through E inferred from the Stoneley wave
 275 analysis (Fig. 4).

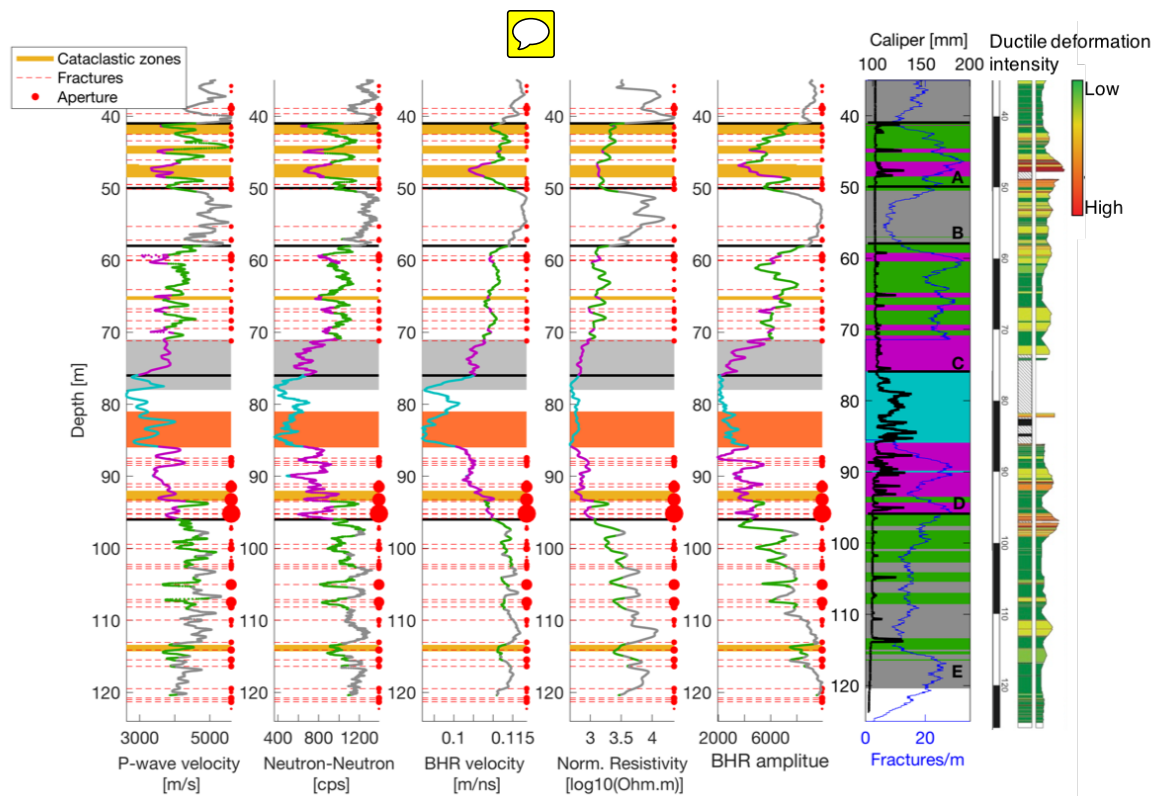


Figure 7. Borehole log data used for cluster analysis color-coded according to the four cluster groups identified in Fig. 6 and overlain by brittle deformation inferred from the OTV data. The right-hand column shows the sequence of clusters along the borehole together with the fracture density inferred from the OTV data, the ductile deformation intensity log (Egli et al., 2018), the caliper data as well as the zonation A through E inferred from the Stonely wave analysis (Fig. 4).

Interestingly, the P-wave velocities and normal resistivity data exhibit a larger variability for cluster 4 than the other petro-physical properties. This becomes especially apparent in zone B, which exhibits a comparatively low fracture density and variable degrees of ductile deformation (Fig. 7). In this partially intact zone, the P-wave velocity assumes maximum and minimum values of 5600 and 4600 m/s, respectively. The former is close to P-wave velocities of non-fractured granitic rocks, which typically range between 5700 and 6200 m/s (e.g., Holbrook et al., 1992; Salisbury et al., 2003). The variability of the P-wave in these more intact zones might thus be an indication of variations in the ductile rock fabric. We also observe strong fluctuations in electrical resistivity and relatively low resistivity values on average for a granitic environment. The latter may point towards the influence of surface conductivity, most likely due to the abundance of mica notably in the gneissic and mylonitic parts of the formation, which, in turn, may result in regions of elevated conductivity compared to the unaltered granites (Keys and Sullivan, 1979). This variability of the P-wave velocity and resistivity is also reflected in the natural gamma log, which, in turn, points to the potential influence of mineralogical changes associated with ductile deformation.



5 Porosity distribution and fluid flow characteristics

Although the borehole logging data are clearly related to the degree of fracturing, which is expected to be a proxy for fluid
290 flow, a quantitative analysis in terms of key hydraulic properties, such as porosity and permeability, in the studied environment
is challenging. The reasons are manifold. As previously mentioned, the Stoneley wave data is not of sufficient quality to
allow for corresponding permeability estimations. The Gamma-Gamma and Neutron-Neutron logs, which are classically used
to determine the porosity via the density and the hydrogen content, respectively, are affected by the large variations in the
borehole diameter. These breakouts make a calibration of the Gamma-Gamma log to obtain density and subsequently porosity
295 essentially impossible. The Neutron-Neutron log is less affected by the caliper variations than the Gamma-Gamma log, but
calibrating it is still difficult due to its non-linear relation to the hydrogen content and the lack of representative core material
over a large enough porosity range. The resistivity logs, cannot not be converted into porosity, since the fluid resistivity is
very high compared to common groundwater, the matrix porosity is quite low, and the surface conductivity cannot be ignored,
which renders Archie's law inapplicable (e.g., Glover, 2015). To circumvent these problems, we utilize the 2015 BHR velocity
300 measurements to derive porosity estimates. This approach is quite robust, since the method is strongly sensitive to the water
content and has a large support volume, which makes it less susceptible to borehole breakouts. The resulting smooth porosity
profile will be then used to calibrate the Neutron-Neutron log, which provides a detailed downscaled version of the porosity
distribution along the borehole. In a subsequent step, we examine the fluid flow characteristics of the subsurface region based
on a combined analysis of the SP, temperature, and resistivity logs.

305 5.1 Porosity estimation

The porosity ϕ is obtained from the BHR velocity v using the so-called Complex Refractive Index Method (CRIM)

$$\phi = \frac{\sqrt{\epsilon_r} - \sqrt{\epsilon_s}}{\sqrt{\epsilon_w} - \sqrt{\epsilon_s}} \text{ with } \sqrt{\epsilon_r} = \frac{v}{c}, \quad (1)$$

where c is the speed of light and v the velocity of the formation, ϵ_r , ϵ_w , and ϵ_s are the relative dielectric permittivities of
the formation, the pore water, and the solid material, respectively (e.g., Greaves et al., 1996). For low porosities, the method
310 is quite sensitive to the dielectric permittivity of the solid material ϵ_s . To find a representative value for ϵ_s , we constrain the
possible range by laboratory-based density measurements. Archimedes-type density measurements have been performed along
the entire core recovered from the GDP1 borehole. These measurements were taken at 20 to 30 cm intervals (personal com-
munication Jürg Renner). The inferred densities are compared to densities calculated from BHR porosities for different values
of ϵ_s (Fig. 8a) using an average grain density of 2653 kg/m³ determined from corresponding laboratory analysis of 8 samples
315 measured. Subsequently, an upper and lower bound for ϵ_s is chosen so that the laboratory-measured densities from competent
samples fall between the resulting calculated density values from the BHR velocities. This provides well-constrained bounds
for low and intermediate porosities. However, the estimation of high porosities is less reliable due to core loss and poor quality
of the retrieved core material from the heavily fractured zones. The results are shown in Fig. 8b together with the porosity



320 curve for the median of the best-fitting dielectric permittivity. For the latter, we only consider the zones without borehole en-
largements.

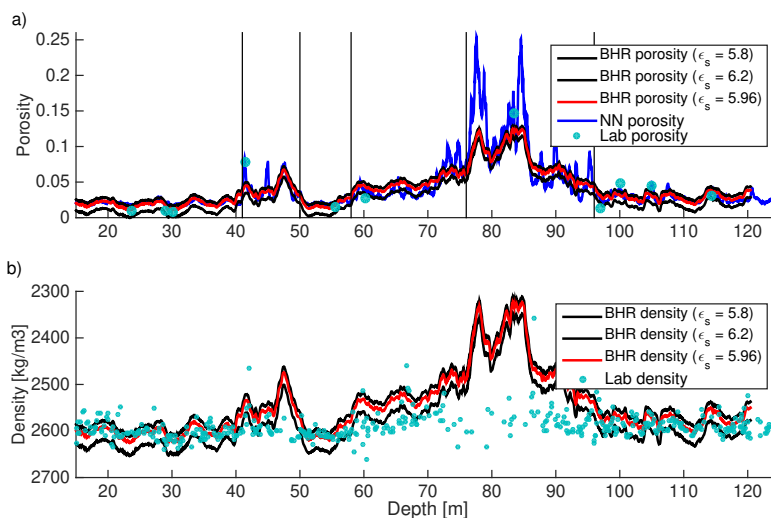


Figure 8. Porosity estimates from BHR velocities for different dielectric permittivities of the solid material ϵ_s and from Neutron-Neutron (NN) data compared with laboratory-based measurements for selected core samples (personal communication Jürg Renner). b) Inferred density from BHR porosities compared to Archimedes-type density measurements on the core samples (personal communication Jürg Renner).

The resulting porosity logs obtained from the BHR velocity measurements are, as expected, smooth due to the method's large support volume and, hence, the strong fluctuations in response to the intense fracturing observed in other borehole logs are averaged out. To capture the variability of the porosity on a smaller scale, the Neutron-Neutron measurements are utilized
325 to downscale the BHR porosity. Details are given in Appendix A. The resulting downscaled porosity log is compared to laboratory-measured porosities for selected core samples (Fig. 8) and to a multi-scale porosity analysis of Egli et al. (2018), which includes OTV data, thin sections, and He-pycnometry (Fig. 9a). Across all these different methods, the corresponding porosity estimates agree remarkably well. Figure 9b shows the sequence of brittle deformation groups inferred from the cluster analysis for comparison along the borehole. The largest porosities prevail, as expected, in the main fault core with a decreasing
330 trend away from this zone. Other high-porosity zones are associated with cataclastic zones and large aperture fractures. Even in the most intact zones, the porosity is, however, still higher than common values of the matrix porosity in crystalline rocks of $\sim 1\%$ or less (Schmitt et al., 2003).

5.2 Fluid flow characteristics

The prevailing fracture network and high-porosity zones associated with brittle deformation are the main flow pathways of the
335 GBF system in its present state. To shed more light on the hydraulic characteristics of this system, we analyze a combination

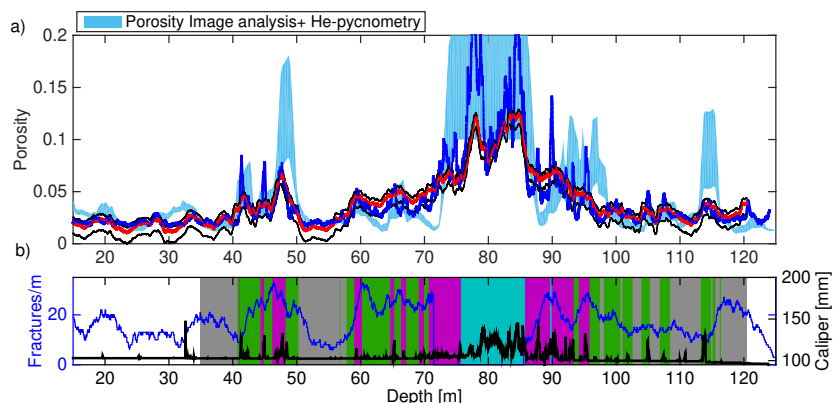


Figure 9. Comparison of log-based porosity estimates with corresponding values from thin section image analysis and He-pycnometry (Egli et al., 2018) and b) brittle deformation groups inferred from cluster analysis (Figs. 6 and 7) with the caliper log and OTV-based fracture density log superimposed.

of SP logs from 2016 and 2017 in conjunction with temperature and fluid resistivity logs. The first part of this sub-section describes the processing and interpretation of the SP data, while the second part focuses on the combined interpretation of the various log data with respect to the fluid flow characteristics.

5.2.1 Self-potential data

340 The SP logs were acquired in the same logging run as the normal resistivity and single-point resistance logs. In this setup, the reference electrode for the SP measurements is the steel cable along which the logging tool is suspended. This causes a very strong drift in the measurements until ~ 30 m of the exposed steel cable is below the water level, afterwards the measurements start to stabilize. For this reason, we only show measurements from 60 m borehole depth onwards for the 2016 and 2017 SP logs, as the water table was at 33 m borehole depth at the time of the measurements. To compensate for the remaining
345 drift of the data, we removed a linear background trend (Appendix B). The resulting logs are shown in Fig. 10 and compared to the open-hole measurements at the bottom of the section acquired in 2017. There are some differences in the absolute values between the open- and cased-hole measurements, however, the main features of the data, especially the position and the character of the anomalies are the same. Overall, the anomalies of the SP logs along the entire considered depth range are pronounced and well defined and show remarkable repeatability between the data acquired in 2016 and 2017.

350

SP anomalies can be of electrokinetic, electrochemical, and thermoelectric origin (e.g., Jackson, 2015). In the studied fractured hydrothermal environment, SP anomalies are most likely of electrokinetic origin. This assessment is supported by an analysis of flowmeter data by Cheng and Renner (2017), which identified zones of in- and outflow into the borehole associated with hydraulically open fractures. For SP signals of electrokinetic origin, the corresponding streaming potential φ can be linked

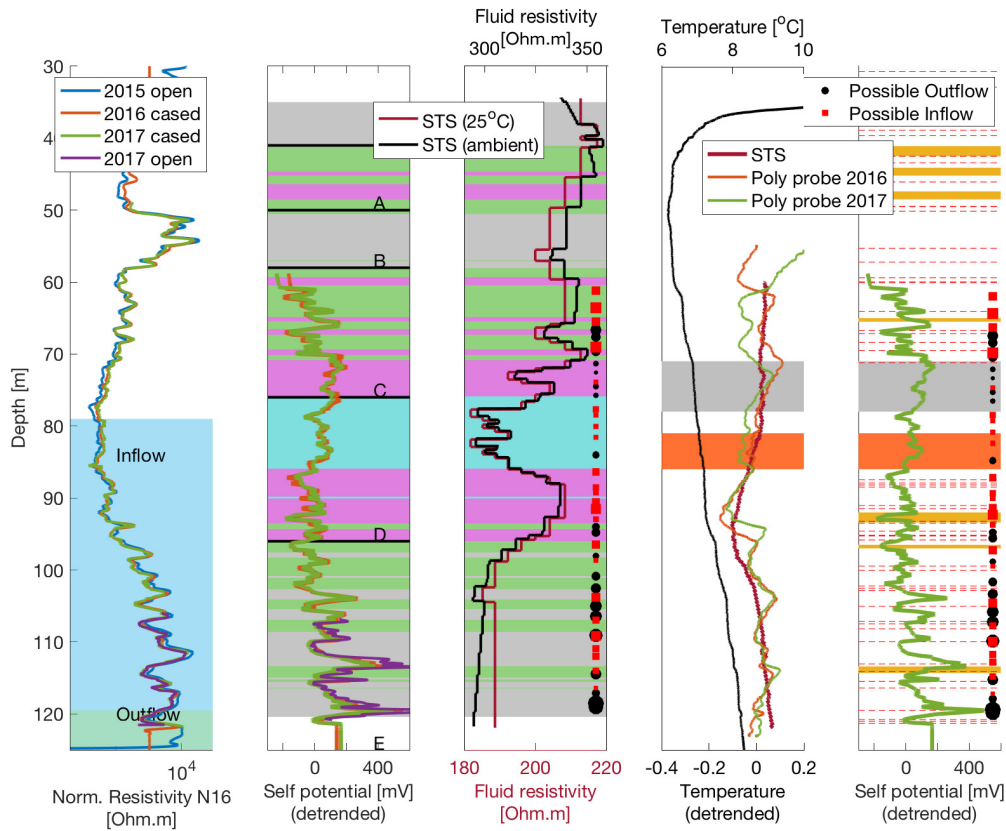


Figure 10. Comparison of the trend-corrected SP data with complementary borehole logs. From left to right: Electrical resistivity and zones of in- and outflow inferred from flowmeter tests (Cheng and Renner, 2017), results of cluster analysis (Fig. 6 and 7) overlain with the detrended SP data, the fluid resistivity log measured in 2016, the temperature logs, and the OTV-based brittle deformation logs (Egli et al., 2018) overlain by the SP data. The fluid resistivity measurements are shown at ambient conditions and corrected to a constant temperature of 25°C. The detrended temperature logs of the polyprobe tool (2016, 2017) and the STS tool (2016) as well as the not trend-corrected temperature profile (black line) acquired with the STS (2016) tool are displayed.

355 to first order to the hydraulic pressure gradient Δp (e.g., Jackson, 2015)

$$\Delta\varphi = C\Delta p, \quad (2)$$

where $C < 0$ is the electrokinetic coupling coefficient. The magnitude of C depends on several factors. Notably, it scales with the electrical conductivity of the pore water over several orders-of-magnitude, thus justifying a simple empirical relation derived from laboratory data for estimating the coupling coefficient for field observations (Revil et al., 2003). Given that, at
 360 ambient conditions, the average fluid resistivity along the GDP1 borehole is ~ 320 Ohm.m (Fig. 10), which is high compared to common groundwater, this results in a large coupling coefficient of ~ -6600 mV/MPa. This, in turn, can explain the large magnitudes of the observed SP anomalies, even in the presence of moderate to weak hydraulic pressure gradients. The high



resistivity of the water in the borehole is not unusual for the area. The adjacent lake water, which has a direct glacial inflow and mostly consists of melt water, has a resistivity of ~ 500 Ohm.m.

365

Figure 10 shows that the observed SP anomalies are abundant and reach values of up to 400 mV, which is indeed very large for signals of electrokinetic origin. Using the above estimate for the coupling coefficient of $C \approx -6600$ mV/MPa, the largest SP anomalies in our data, imply hydraulic pressure gradients of the order of 0.06 MPa. This is approximately one order-of-magnitude lower than the pressure gradients estimated by Suski et al. (2008) in a saline artesian fractured hydrothermal system for maximum SP anomalies of ~ 50 m. Despite their unusually large magnitudes for SP signals of electrokinetic origin, the anomalies observed along the GDP1 borehole thus seem to be realistic for the specific setting. Indeed, SP anomalies of similar magnitude were recorded in the Grimsel Underground Laboratory (Himmelsbach et al., 2003), which is situated in the same granitic formation ~ 400 m below the Grimsel Pass. In this case, the anomalies could be attributed to electrokinetic responses of distinct fractures. An additional contribution to the measured SP signals along the GDP1 borehole could arise from variations in the bulk resistivity. This might come into play between 95 to 120 m borehole depth, where we observe relatively strong variations in resistivity, which are linked to the variable degree of fracturing, as illustrated by the results of the cluster analysis (Fig. 7).

Considering the described uncertainties and the abundance of SP anomalies due to the intensely fractured nature of the formation, associating a single anomaly deterministically with in- or outflow is impossible. To overcome this problem, we apply a probability tomography based on Di Maio and Patella (1994). This approach reconstructs an image of the most probable locations of SP sources, which explain the observed data by assuming that an anomaly measured at location \vec{r} can be represented by a linear superposition of partial SP effects due to elementary electric source elements located at \vec{r}_q . For the considered borehole measurements, we scan a region which cuts the borehole along its trajectory for such source elements with the scanning function

385

$$S_c(\vec{r}, \vec{r}_q) = \frac{\overrightarrow{r}_q(x, z) - \overrightarrow{r}(x, z)}{|\overrightarrow{r}_q(x, z) - \overrightarrow{r}(x, z)|^3} \quad (3)$$

The result of this procedure is an electric charge occurrence probability (ECOP) map given by the cross-correlation between the scanning function and the electrical field associated with the SP measurements. For SP signals caused by a distribution of dipole sources, corresponding dipole occurrence probability (DOP) maps can be calculated for the horizontal and vertical component of the dipoles. A more detailed description of the method is given by Hämman et al. (1997); Mauriello and Patella (1999); Iuliano et al. (2002) and Saracco et al. (2004).

Figures 11a and 11b show the resulting ECOP and DOP for the largest of the two dipole components at each location along the borehole track. The DOP map is overlain by DOP vectors constructed from the horizontal and vertical dipole components. These vectors are indicative of the direction of fluid flow at a specific location. For display purposes, a threshold has been chosen and only vectors with an absolute probability larger than 0.15 are shown. Also shown are the most probable vectors,

395

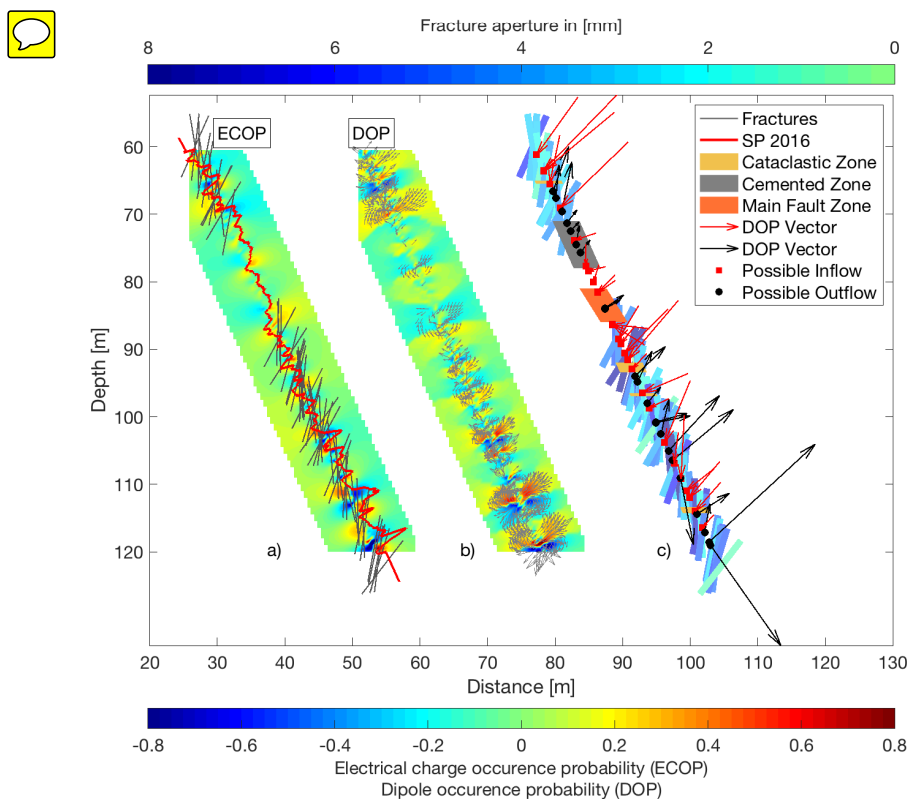


Figure 11. a) Electric charge occurrence probability (ECOP) and b) dipole occurrence probability (DOP) maps along the borehole track overlain by the SP log and fractures from OTV data, and DOP vectors with an absolute probability larger than 0.15, respectively. c) Most probable DOP vectors in each 1.2 m interval mapped onto the borehole track together with a projection of fracture planes and their color-coded apertures.

which are selected in subsequent 1.2 m intervals and mapped onto the borehole trajectory together with the orientation and aperture of the fractures identified from the OTV data in Fig. 11c. Positive and negative values in the ECOP map indicate regions that gain and loose water, respectively, as such they are possible locations of in- and outflow along the borehole. The
400 selected DOP vectors in Fig. 11c are color-coded correspondingly and indicate possible in- and outflow scenarios. For the interpretation of the hydraulic behavior, we focus on these scenarios.

5.3 Hydraulic zonation

The observed SP anomalies can be associated with fractures and cataclastic zones identified in the OTV data (Fig. 10). The representative DOP vectors and corresponding ECOP values indicate that above 95 m borehole depth inflow is dominating.
405 Inflow into the borehole can be caused by flow from fractures and downflow along the borehole. Both scenarios are likely to



occur. The former is supported by DOP vectors coinciding with the direction of the fracture dip suggesting flow along fractures and the latter by flowmeter measurements conducted in 2015 indicating a generic downflow regime along the entire borehole. Below ~ 95 m borehole depth, the character of the SP data and the associated DOP vectors and ECOP values are more variable, including both inflow and outflow with an increase of the number of outflow regions towards the bottom of the borehole and
410 a dominant outflow around 120 m borehole depth. These observations are generally consistent with results from flowmeter measurements and an analysis of natural hydraulic heads by Cheng and Renner (2017). They identified inflow between 81 and 119 m and a zone of prominent outflow below 119 m borehole depth, as indicated by the blue and green rectangles in Fig. 10.

With regard to the zonation derived from the analysis of Stoneley waves (Fig. 4), the relevant zones in the given context are
415 C, D, and E (Fig. 10). Zone C consists of partially non-cohesive core material and contains a number of individual fractures of large apertures, zone D is the wider zone of the main fault core, which is largely brecciated, and zone E is represented by more compact rock with prominent individual fractures. The largest SP anomalies are observed in zone E and some distinct signals in zone C, whereas the zone around the main fault core shows much less variability and smaller anomalies. This suggests that zones of in- and outflow are likely to be dominated by individual fractures or localized fracture clusters. Furthermore, the fluid
420 resistivity shows a very distinct layering along the borehole track (Fig. 10). Although, the corresponding variations are not large in magnitude, they clearly imply distinct variations in salinity, which, in turn, points to differing origins and flow paths of the water in the borehole. Potential sources of water in the steeply dipping, fracture-dominated geological structure around the GBF may comprise direct infiltration of meteoric water through the outcropping parts of the GBF, shallow groundwater flow, and upflow from greater depth along the GBF zone. There is a hydraulic connection between the Transitgas AG tunnel
425 and the GDP1 borehole, as evidenced by polymers from the drilling operation found in the tunnel. Two zones with relatively low fluid resistivities prevail around the main fault core (cluster 1) and below 95 m borehole depth, whereas above the main fault core and in the intensely fractured interval between 85 to 95 m borehole depth relatively high fluid resistivities are observed. The latter coincide with a small low-temperature anomaly in the detrended temperature data. These observations suggest infiltration of meteoric water along the fracture network in the more resistive zones, whereas in the other zones inflow
430 of more mineralized water, possibly from greater depth, occurs. All of this points to the presence of distinctively different sources and passages of fluid flow in the studied subsurface region of the GBF, thus suggesting a compartmentalization of fluid pathways in the larger-scale hydraulic system.

6 Discussion

The BHR reflection image reveals a network of fluid-filled fractures in the damage zones above and below the main fault core.
435 A projection of the reflections identified in this image onto the borehole track is shown in Fig. 12. Reflections with relative dips above 55° are well captured by the image and in good agreement with the interpretation of the OTV data. Conversely, events with smaller dips are more difficult to detect due to the single-hole setup and the limited offset. The extent and continuity of reflections away from the borehole can only be assessed in zones with low signal attenuation, as evidenced by high first-



440 cycle amplitudes. High signal attenuation, as evidenced by low first-cycle amplitudes, occurs in several zones characterized by intense brittle deformation. This also prevents a more quantitative analysis of the reflection amplitudes, which could be theoretically related to fracture apertures in a more favorable environment.

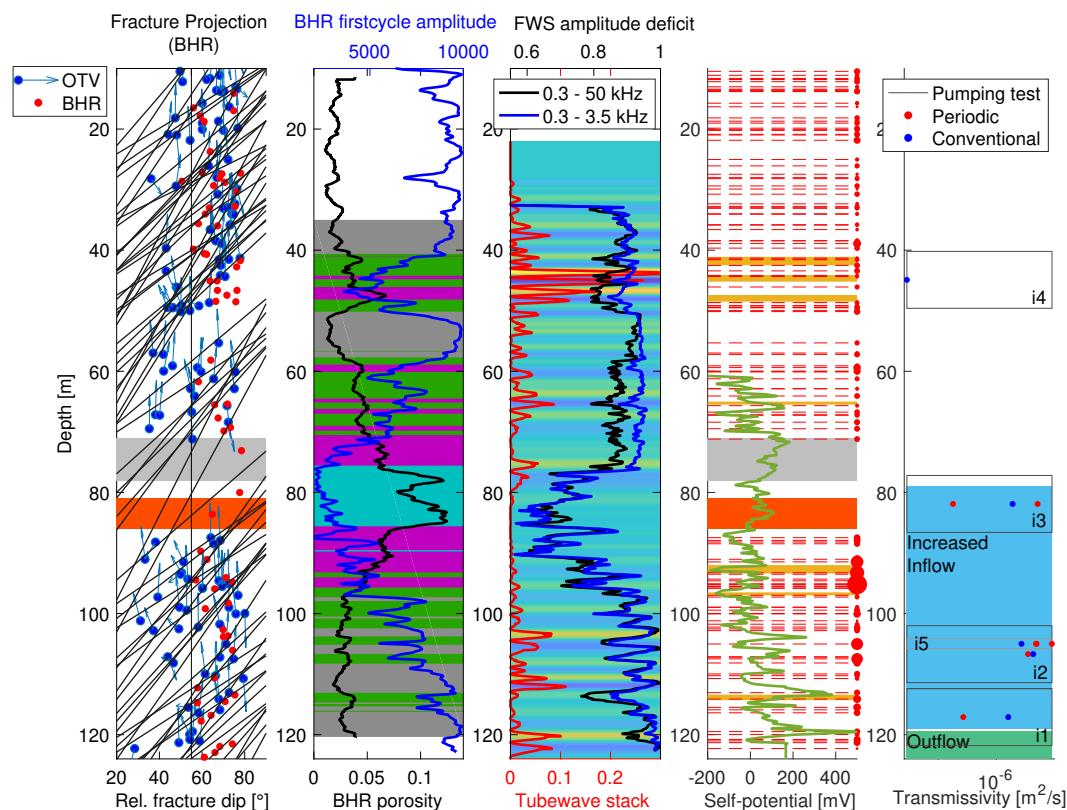


Figure 12. From left to right: Projection of imaged BHR reflections onto the borehole track together with associated dip, tadpoles illustrating the azimuth and dip for the fractures identified from the OTV data; results of cluster analysis overlain by BHR porosity and BHR amplitudes; tubewave stack overlain by tube wave energy (Greenwood et al., 2019) and Stoneley energy deficit; brittle deformation data overlain by the corrected SP log (2017); and summary of transmissivities estimated from pumping tests (Cheng and Renner, 2017).

445 For specifically targeted zones, indicated in Fig. 12, Cheng and Renner (2017) performed conventional and periodic pumping tests in the GDP1 borehole in 2015. The resulting transmissivity estimates are shown in Fig. 12. The highest values are obtained for the intervals i2 and i5, which feature a large aperture fracture at 105 m borehole depth. This fracture can be associated with a distinct anomaly in the SP data and the energy deficit. However, no clear trend can be established between the magnitude of the anomalies in the two log attributes and the estimated transmissivity from the pumping tests. One reason is that the pumping test only provides a few values of transmissivity averaged over relatively large intervals. The logs analyzed in this study do,



Table 3. Petrophysical properties of the cluster groups (25th and 75th percentile) and core measurements

Cluster analysis	Cluster 1	Cluster 2	Cluster 3	Cluster 4	Drill core
Porosity [%]					0.84 - 14.73*
BHR	9 - 12	4.7 - 6.6	3 - 4	1.8 - 2.8	
Neutron-Neutron	10 - 16 (max: 26)	4.5 - 6.9 (max: 12.2)	2.8 - 3.5	2 - 2.5 (min: 1.6)	
P-wave velocity [m/s]	2920 - 3377 (min: 2613)	3548 - 3849	4056 - 4482	4464 - 5013 (max: 5603)	5386 - 5861** (4657 - 5448)
S-wave velocity [m/s]	1878 - 2225 (min: 1732)	2135 - 2352	2347 - 2549	2523 - 2744 (max: 3024)	2952 - 3380**
Rock type	Fault breccia	Cataclasite	Mylonite/Ultramylonite	Gneiss	Granite
Mean matrix and micro-fracture porosity*** [%]	14.8	10.8	3 - 4	2.3	0.9

*personal communication Jürg Renner,** Ultrasonic measurements for saturated (and dry) samples under ambient conditions (personal communication Jürg Renner), *** Egli et al. (2018) Multi-scale analysis

however, point to a compartmentalized system with multiple distinct hydraulic zones. This is consistent with the results of Cheng and Renner (2017), which suggest a complex and variable flow geometry on the decameter scale associated with a heterogeneous system dominated by steeply dipping structures with a pipe-like hydraulic behavior. This interpretation is also supported by the study of Belgrano et al. (2016), who analyzed the architecture and hydrothermal activity of the GBF with emphasis on fluid pathways at different scales. They concluded that the hydraulic characteristics are controlled by localized sub-vertically oriented pipe-like upflow zones.

7 Conclusions

With the objective to characterize the fracture network of the damage zone surrounding the GBF and its petrophysical properties, we have performed an integrated analysis of the geophysical borehole log measurements. Although the log data are affected by challenging borehole conditions, notably numerous and large breakouts, the dataset contains a multitude of valuable information, which is in agreement with previous studies and adds to their findings. The BHR reflection data in combination with the OTV data suggest a complex network of fluid-filled fractures in the damage zone surrounding the main fault core of the GBF. Larger-scale fractures can be tracked several meters into the formation in the BHR reflection image, which, in turn, confirms that the borehole breakouts can generally be related to geological features and are not primarily drilling-induced damage. A comparison of the borehole logs to the fracture characteristics inferred from the OTV data confirms that the response of the logs and, thus the variations in petrophysical properties, are predominantly governed by the intensity of brittle deformation. A clear influence of ductile deformation on the petrophysical properties cannot be discerned. Overall, the measured petrophysical properties correlate very well with each other. Many of the petrophysical properties show distinctly different values than



those expected for intact granitic formations, such as P-wave and S-wave velocities ranging between 2600 m/s to 5600 m/s and 1600 m/s to 3200 m/s, respectively, and porosities ranging between 3 % and 15 %. The compliant high-porosity zones associated with cataclastic structures and fractures are the main fluid pathways of the system. The SP data show an abundance of anomalies, which can be linked to fractures and are most likely of electrokinetic origin. The results of the SP probability tomography suggest that above 95 m inflow is dominating and below inflow and outflow occurs with a dominant outflow region around 120 m borehole depth. Furthermore, the distinct layering observed in the fluid resistivity points to a compartmentalized pipe-like hydraulic behavior dominated by the steeply dipping geological structures as well as to the inflow of water from various different sources.

475 Appendix A

To derive reliable porosity estimates from the first-arrival travel times of the BHR data, we have to apply a zero-time correction. For the data collected in 2015, a zero-time correction was not available. Thus, we used the corresponding information for the 2016 data (Fig. A1) to first correct the 2016 picks (Fig. A2). This is followed by a static shift of the 2015 picks corresponding to the mean difference in travel times with regard to the corrected 2016 picks. The resulting corrected travel times of the 2015 BHR data are shown in Fig. A2 and are used for the porosity estimation in Sec. 5.1.

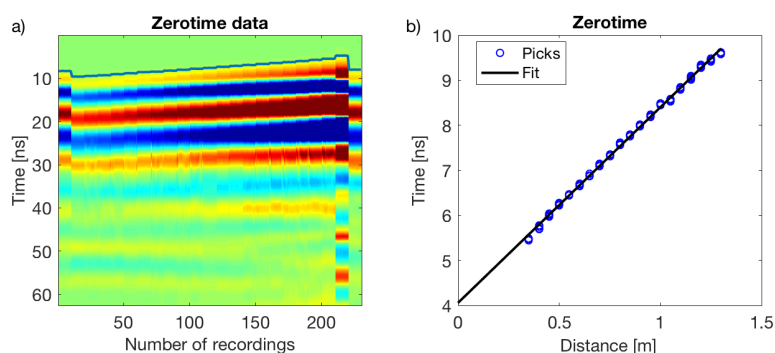


Figure A1. a) Data collected in 2016 for zero-time correction showing 10 recordings per distance as well as the first arrival picks. b) Picked first arrivals vs distance with the corresponding linear regression fit. First and last 10 stacks are not considered.

To downscale the porosity estimates obtained from the BHR data, we utilize the Neutron-Neutron log. Therefore, we calibrate the Neutron-Neutron log with the BHR porosity estimates above and below the main fault core by fitting a power law relationship. The calibration interval is shown in Fig. A3a and the resulting fit in Fig. A3b. The data in Fig. A3b is displayed in terms of a histogram crossplot. For comparison, we have also plotted porosities measured in the laboratory for selected core samples, which are in good agreement with the data fit. Subsequently, we used the inferred power law to convert the counts of the Neutron-Neutron log into porosities along the entire borehole.

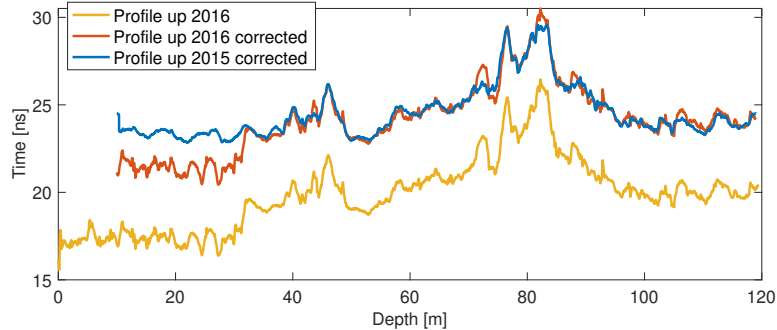


Figure A2. Comparison of zero-time corrected travel times of the 2015 and 2016 BHR data.

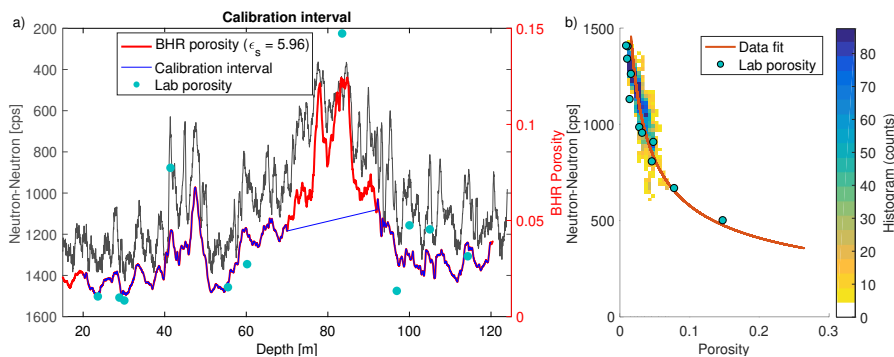


Figure A3. a) Neutron-Neutron counts and best-fitting BHR porosity. b) Fitted relation between the Neutron-Neutron and the BHR porosity overlaying a corresponding histogram crossplot.

Appendix B

490 The resistivity logs were acquired in three consecutive years. The 2015 data correspond to open-hole conditions. They are affected by the pumping of lake water into the borehole as well as by the remnants of polymer-based drilling mud in the formation. Conversely, the 2016 and 2017 data were measured through slotted PVC casing. As a result, the logs contain spikes at the positions of the casing joints as illustrated in Fig. B1 for the normal resistivity, single point resistance, and SP data. We corrected the data by removing the spikes and subsequent linear interpolation of the gaps. For the normal resistivity data, we
495 recovered the variability of the logs by replacing the interpolated sections with the 2015 data shifted to the respective baseline of the 2016 or 2017 data (Toschini, 2018). The resulting logs are shown in Fig.B2.

The SP measurements are additionally affected by a very strong drift, since the steel cable suspending the tool serves as the reference electrode. The data is unusable until the exposed cable is ~ 30 m below the water level. Since the water table was
500 at 33 m borehole depth at the time of the measurements in 2016 and 2017, the logs can only be used from ~ 60 m onwards.

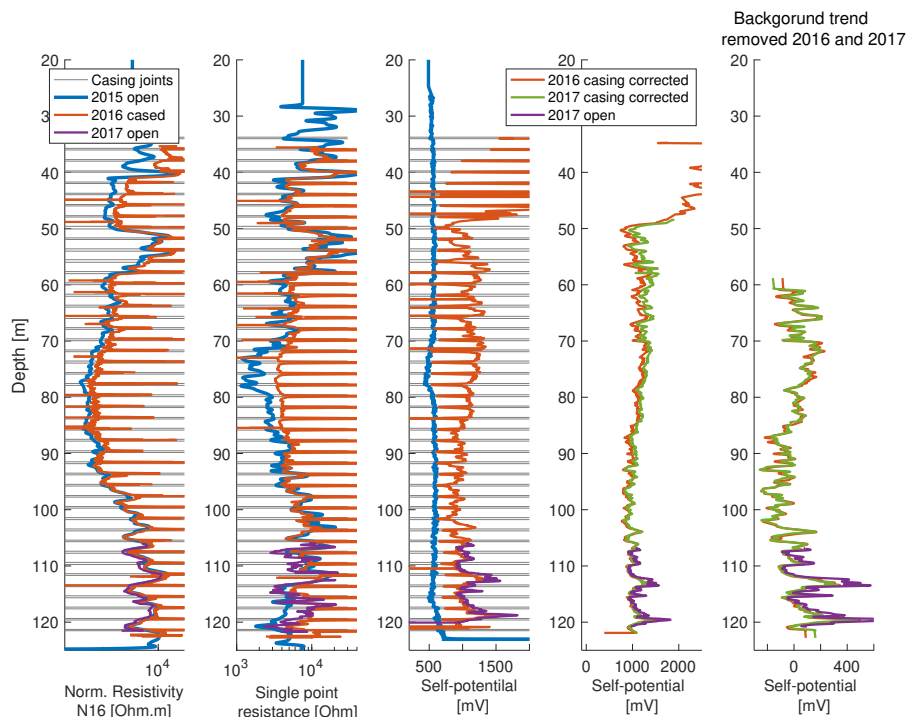


Figure B1. Comparison of open- and cased-hole data. From left to right: normal resistivity, single-point resistance, and SP logs for 2015, 2016 and 2017 with casing joints marked in grey, casing-corrected SP log, and background-trend-corrected SP log.

To compensate for the remaining drift in the data below ~ 60 m borehole depth, we remove a linear background trend for each dataset separately instead of normalizing the data to a constant baseline value (Fig.B1).

Figure B2 shows a selection of the casing-corrected resistivity data measured in 2016 and 2017 in comparison to the 2015
505 open-hole data. Across all three years, the normal resistivity (N16) measurements are consistent. The biggest differences occur in the high-porosity zone A and around the cementation region of the borehole. The most likely reason is a change in water resistivity possibly due

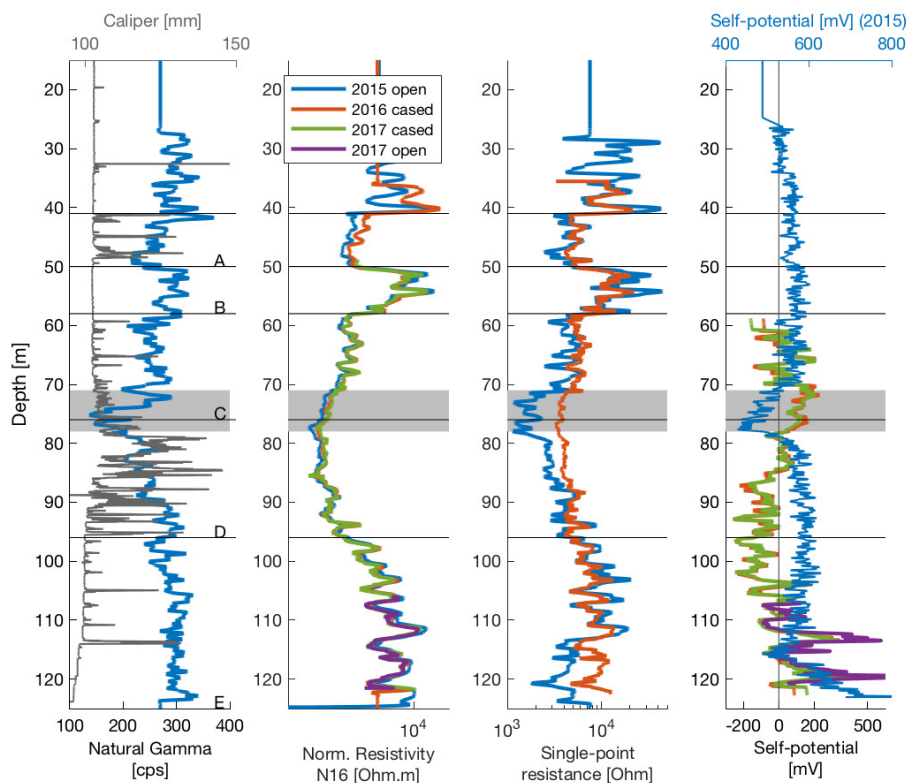


Figure B2. Comparison of open-hole and casing-corrected resistivity logs.

Data availability. The data will be deposited in an open-access database. They are currently available upon request.

Competing interests. The authors declare that they have no conflict of interest.

- 510 *Author contributions.* Eva Caspari: Data processing, analysis and interpretation, preparation of the manuscript
Andrew Greenwood: Data acquisition and conditioning, processing of borehole radar data and contribution to the overall data interpretation
Ludovic Baron: Design of the logging campaign, data acquisition and support with the data analysis
Daniel Egli: Geological interpretation, analysis of the OTV data and porosity estimation from image analysis
Enea Toschini: Acquisition and processing of the normal resistivity data
515 Kaiyan Hu: Probability tomography of the self potential data and support with the interpretation of the self potential data
Klaus Holliger: Project leadership, contributions to data interpretation and manuscript preparation

<https://doi.org/10.5194/se-2019-151>

Preprint. Discussion started: 11 November 2019

© Author(s) 2019. CC BY 4.0 License.



Acknowledgements. This work was supported by the Swiss National Science Foundation through the National Research Programme 70 “Energy Turnaround” and completed within the Swiss Competence Center on Energy Research – Supply of Electricity, with the support of the Swiss Innovation Agency. We thank Tobias Zahner for his active involvement in the 2015 and 2016 data acquisition campaign, Yannick
520 Forth and Jörg Renner from Ruhr-University Bochum for providing Archimedes type density measurements and porosity measurements performed on the core samples, and Jörg Renner for the ultrasonic velocity measurements.



References

- Arthur, D. and Vassilvitskii, S.: k-means++: The advantages of careful seeding, in: Proceedings of the eighteenth annual ACM-SIAM symposium on Discrete algorithms, pp. 1027–1035, Society for Industrial and Applied Mathematics, 2007.
- 525 Barbosa, N. D., Caspari, E., Rubino, J. G., Greenwood, A., Baron, L., and Holliger, K.: Estimation of fracture compliance from attenuation and velocity analysis of full-waveform sonic log data, *Journal of Geophysical Research: Solid Earth*, 124, 2738–2761, 2019.
- Barton, C. A., Zoback, M. D., and Moos, D.: Fluid flow along potentially active faults in crystalline rock, *Geology*, 23, 683–686, 1995.
- Belgrano, T. M., Herwegh, M., and Berger, A.: Inherited structural controls on fault geometry, architecture and hydrothermal activity: an example from Grimsel Pass, Switzerland, *Swiss Journal of Geosciences*, 109, 345–364, 2016.
- 530 Berkowitz, B.: Characterizing flow and transport in fractured geological media: A review, *Advances in Water Resources*, 25, 861–884, 2002.
- Brace, W.: Permeability of crystalline and argillaceous rocks, in: *International Journal of Rock Mechanics and Mining Sciences & Geomechanics Abstracts*, vol. 17 (5), pp. 241–251, Elsevier, 1980.
- Caine, J. S., Evans, J. P., and Forster, C. B.: Fault zone architecture and permeability structure, *Geology*, 24, 1025–1028, 1996.
- Cheng, Y. and Renner, J.: Exploratory use of periodic pumping tests for hydraulic characterization of faults, *Geophysical Journal International*, 212, 543–565, 2017.
- 535 Di Maio, R. and Patella, D.: Self-potential anomaly generation in volcanic areas. The Mt. Etna case-history. *Acta Vulcanol*, 4, 119–124, 1994.
- Dorn, C., Linde, N., Doetsch, J., Le Borgne, T., and Bour, O.: Fracture imaging within a granitic rock aquifer using multiple-offset single-hole and cross-hole GPR reflection data, *Journal of Applied Geophysics*, 78, 123–132, 2012.
- 540 Egli, D., Baumann, R., Küng, S., Berger, A., Baron, L., and Herwegh, M.: Structural characteristics, bulk porosity and evolution of an exhumed long-lived hydrothermal system, *Tectonophysics*, 747, 239–258, 2018.
- Ellis, D. V. and Singer, J. M.: *Well logging for earth scientists*, vol. 692, Springer, 2007.
- Evans, J. P., Forster, C. B., and Goddard, J. V.: Permeability of fault-related rocks, and implications for hydraulic structure of fault zones, *Journal of structural Geology*, 19, 1393–1404, 1997.
- 545 Evans, K. F., Genter, A., and Sausse, J.: Permeability creation and damage due to massive fluid injections into granite at 3.5 km at Soultz: 1. Borehole observations, *Journal of Geophysical Research: Solid Earth*, 110, 2005.
- Faulkner, D. and Armitage, P.: The effect of tectonic environment on permeability development around faults and in the brittle crust, *Earth and Planetary Science Letters*, 375, 71–77, 2013.
- Genter, A., Castaing, C., Dezayes, C., Tenzer, H., Traineau, H., and Villemin, T.: Comparative analysis of direct (core) and indirect (borehole
550 imaging tools) collection of fracture data in the Hot Dry Rock Soultz reservoir (France), *Journal of Geophysical Research: Solid Earth*, 102, 15 419–15 431, 1997.
- Glover, P.: Geophysical properties of the near surface Earth: Electrical properties, in: *Treatise on Geophysics (Second Edition)*, pp. 89–137, Elsevier, 2015.
- Greaves, R. J., Lesmes, D. P., Lee, J. M., and Toksöz, M. N.: Velocity variations and water content estimated from multi-offset, ground-
555 penetrating radar, *Geophysics*, 61, 683–695, 1996.
- Greenwood, A., Caspari, E., Egli, D., Baron, L., Zahner, T., Hunziker, J., and Holliger, K.: Characterization and imaging of a hydrothermally active near-vertical fault zone in crystalline rocks based on hydrophone VSP data, *Tectonophysics*, 750, 153–176, 2019.



- Hämmann, M., Maurer, H., Green, A., and Horstmeyer, H.: Self-potential image reconstruction: capabilities and limitations, *Journal of Environmental and Engineering Geophysics*, 2, 21–35, 1997.
- 560 Himmelsbach, T., Shao, H., Wiczorek, K., Flach, D., Schuster, K., Alheid, H.-J., Liou, T.-S., Bartlakowski, J., and Krekeler, T.: Grimsel Test Site Investigation Phase V Effective Field Parameter EFP, TECHNISCHER BERICHT-NAGRA NTB, 2003.
- Hobday, C. and Worthington, M.: Field measurements of normal and shear fracture compliance, *Geophysical Prospecting*, 60, 488–499, 2012.
- Hofmann, B. A., Helfer, M., Diamond, L. W., Villa, I. M., Frei, R., and Eikenberg, J.: Topography-driven hydrothermal breccia mineralization
565 of Pliocene age at Grimsel Pass, Aar massif, Central Swiss Alps, *Schweizerische Mineralogische und Petrographische Mitteilungen*, 84, 271–302, 2004.
- Holbrook, W. S., Mooney, W. D., and Christensen, N. I.: The seismic velocity structure of the deep continental crust, in: *Continental Lower Crust, Developments in Geotectonics*, edited by Fountain, D.M., Arculus, R., and Kay, R.W., pp. 1–43, Elsevier Amsterdam, 1992.
- Hornby, B. E.: Imaging of near-borehole structure using full-waveform sonic data, *Geophysics*, 54, 747–757, 1989.
- 570 Iuliano, T., Mauriello, P., and Patella, D.: Looking inside Mount Vesuvius by potential fields integrated probability tomographies, *Journal of Volcanology and Geothermal Research*, 113, 363–378, 2002.
- Jackson, M.: Tools and techniques: Self-potential methods, in: *Treatise on Geophysics (Second Edition)*, pp. 261–293, Elsevier, 2015.
- Keys, W. S. and Sullivan, J. K.: Role of borehole geophysics in defining the physical characteristics of the Raft River geothermal reservoir, Idaho, *Geophysics*, 44, 1116–1141, 1979.
- 575 Liu, E. and Martinez, A.: Seismic fracture characterization, EAGE, 2014.
- Loew, S., Barla, G., and Diederichs, M.: Engineering geology of Alpine tunnels: Past, present and future, in: *Geologically active—Proceedings of the 11th IAEG Congress*, pp. 201–253, 2010.
- Mauriello, P. and Patella, D.: Resistivity anomaly imaging by probability tomography, *Geophysical Prospecting*, 47, 411–429, 1999.
- Nelson, R.: *Geologic analysis of naturally fractured reservoirs*, Elsevier, 2001.
- 580 Olsson, O., Falk, L., Forslund, O., Lundmark, L., and Sandberg, E.: Borehole radar applied to the characterization of hydraulically conductive fracture zones in crystalline rock 1, *Geophysical Prospecting*, 40, 109–142, 1992.
- Paillet, F. L.: Acoustic characterization of fracture permeability at Chalk River, Ontario, *Canadian Geotechnical Journal*, 20, 468–476, 1983.
- Paillet, F. L.: Application of borehole geophysics in the characterization of flow in fractured rocks, *Water-Resources Investigations Report*, 93, 4214, 1994.
- 585 Prioul, R. and Jocker, J.: Fracture characterization at multiple scales using borehole images, sonic logs, and walkaround vertical seismic profile, *AAPG Bulletin*, 93, 1503–1516, 2009.
- Regenauer-Lieb, K., Bungler, A., Chua, H. T., Dyskin, A., Fusses, F., Gaede, O., Jeffrey, R., Karrech, A., Kohl, T., Liu, J., et al.: Deep geothermal: The ‘Moon Landing’ mission in the unconventional energy and minerals space, *Journal of Earth Science*, 26, 2–10, 2015.
- Revil, A., Naudet, V., Nouzaret, J., and Pessel, M.: Principles of electrography applied to self-potential electrokinetic sources and hydrogeo-
590 logical applications, *Water Resources Research*, 39, 2003.
- Salisbury, M. H., Harvey, C. W., Matthews, L., Eaton, D., and Milkereit, B.: The acoustic properties of ores and host rocks in hardrock terranes, *Hardrock seismic exploration*. Edited by DW Eaton, B. Milkereit, and MH Salisbury. Society of Exploration Geophysicists, Tulsa, Okla, pp. 9–19, 2003.
- Saracco, G., Labazuy, P., and Moreau, F.: Localization of self-potential sources in volcano-electric effect with complex continuous wavelet
595 transform and electrical tomography methods for an active volcano, *Geophysical Research Letters*, 31, 2004.



- Schmitt, D. R., Mwenifumbo, C. J., Pflug, K. A., and Meglis, I. L.: Geophysical logging for elastic properties in hard rock: a tutorial, *Hardrock seismic exploration*. Edited by DW Eaton, B. Milkereit, and MH Salisbury. Society of Exploration Geophysicists, Tulsa, Okla, pp. 20–42, 2003.
- Sonney, R. and Vuataz, F.-D.: Properties of geothermal fluids in Switzerland: a new interactive database, *Geothermics*, 37, 496–509, 2008.
- 600 Stephens, M. B., Follin, S., Petersson, J., Isaksson, H., Juhlin, C., and Simeonov, A.: Review of the deterministic modelling of deformation zones and fracture domains at the site proposed for a spent nuclear fuel repository, Sweden, and consequences of structural anisotropy, *Tectonophysics*, 653, 68–94, 2015.
- Suski, B., Ladner, F., Baron, L., Vuataz, F.-D., Philipposian, F., and Holliger, K.: Detection and characterization of hydraulically active fractures in a carbonate aquifer: results from self-potential, temperature and fluid electrical conductivity logging in the Combioula hydrothermal system in the southwestern Swiss alps, *Hydrogeology Journal*, 16, 1319–1328, 2008.
- 605 Tibshirani, R., Walther, G., and Hastie, T.: Estimating the number of clusters in a data set via the gap statistic, *Journal of the Royal Statistical Society: Series B (Statistical Methodology)*, 63, 411–423, 2001.
- Toschini, E.: Exploration et caractérisation d’une zone hydrothermale fracturée active: acquisition, traitement et interprétation de mesures géoélectriques dans un puits, Master’s thesis, University of Lausanne, 2018.
- 610 Townend, J., Sutherland, R., Toy, V., Eccles, J., Boulton, C., Cox, S., and McNamara, D.: Late-interseismic state of a continental plate-bounding fault: Petrophysical results from DFDP-1 wireline logging and core analysis, *Alpine Fault, New Zealand, Geochemistry, Geophysics, Geosystems*, 14, 3801–3820, 2013.
- Valley, B. C.: The relation between natural fracturing and stress heterogeneities in deep-seated crystalline rocks at Soultz-sous-Forêts (France), Ph.D. thesis, ETH Zurich, 2007.
- 615 Waber, H., Schneeberger, R., Mäder, U., and Wanner, C.: Constraints on evolution and residence time of geothermal water in granitic rocks at Grimsel (Switzerland), *Procedia Earth and Planetary Science*, 17, 774–777, 2017.